

Journal of  
**Applied Remote Sensing**

RemoteSensing.SPIEDigitalLibrary.org

## **Calibration approach and plan for the sea and land surface temperature radiometer**

David L. Smith  
Tim J. Nightingale  
Hugh Mortimer  
Kevin Middleton  
Ruben Edeson  
Caroline V. Cox  
Chris T. Mutlow  
Brian J. Maddison  
Peter Coppo

# Calibration approach and plan for the sea and land surface temperature radiometer

David L. Smith,<sup>a,\*</sup> Tim J. Nightingale,<sup>a</sup> Hugh Mortimer,<sup>a</sup>  
Kevin Middleton,<sup>a</sup> Ruben Edeson,<sup>a</sup> Caroline V. Cox,<sup>a</sup> Chris T. Mutlow,<sup>a</sup>  
Brian J. Maddison,<sup>a</sup> and Peter Coppo<sup>b</sup>

<sup>a</sup>Rutherford Appleton Lab Space, Science and Technologies Facilities Council,  
Harwell Oxford, OX11 0QX, United Kingdom

<sup>b</sup>Selex-ES, Via. A. Einstein, Florence 35, 50013, Italy

**Abstract.** The sea and land surface temperature radiometer (SLSTR) to be flown on the European Space Agency's (ESA) Sentinel-3 mission is a multichannel scanning radiometer that will continue the 21 year dataset of the along-track scanning radiometer (ATSR) series. As its name implies, measurements from SLSTR will be used to retrieve global sea surface temperatures to an uncertainty of <0.3 K traced to international standards. To achieve, these low uncertainties require an end-to-end instrument calibration strategy that includes prelaunch calibration at subsystem and instrument level, on-board calibration systems, and sustained post-launch activities. The authors describe the preparations for the prelaunch calibration activities, including the spectral response, the instrument level alignment tests, and the solar and infrared radiometric calibrations. A purpose built calibration rig has been designed and built at the Rutherford Appleton Laboratory space department (RAL Space) that will accommodate the SLSTR instrument, the infrared calibration sources, and the alignment equipment. The calibration rig has been commissioned and results of these tests will be presented. Finally, the authors will present the planning for the on-orbit monitoring and calibration activities to ensure that the calibration is maintained. These activities include vicarious calibration techniques that have been developed through previous missions and the deployment of ship-borne radiometers. © The Authors. Published by SPIE under a Creative Commons Attribution 3.0 Unported License. Distribution or reproduction of this work in whole or in part requires full attribution of the original publication, including its DOI. [DOI: [10.1117/1.JRS.8.084980](https://doi.org/10.1117/1.JRS.8.084980)]

**Keywords:** SLSTR; Sentinel-3; calibration; radiometry; infrared; thermal; visible; SWIR.

Paper 14098SSP received Feb. 13, 2014; revised manuscript received May 20, 2014; accepted for publication May 21, 2014; published online Jun. 30, 2014.

## 1 Introduction

The Sentinel-3 mission is one of a series of spacecraft that make up the space segment of the Copernicus program<sup>1</sup> and will measure ocean and land surface parameters. The mission comprises four main instruments: the sea and land surface temperature radiometer (SLSTR), the ocean and land color instrument (OCLI); a dual-frequency (Ku and C band) synthetic aperture radar altimeter (SRAL), and a microwave radiometer.

SLSTR (Fig. 1) will be used to retrieve global sea surface temperatures (SSTs) to an uncertainty of <0.3 K traced to international standards and will continue the twenty-first-year datasets of the along-track scanning radiometer (ATSR) series. SLSTR shares many features of the ATSR sensors including thermal infrared (IR) spectral bands that are cooled using a Stirling cycle cooler, a dual view allowing the same terrestrial scene to be viewed through two atmospheric paths, a nadir view and an along-track view at 55 deg zenith angle, two blackbody (BB) sources to provide continuous calibration of the IR channels, and a diffuser-based visible calibration (VISCAL) source for calibrating the solar reflectance bands. The optical design of the instrument is a development of the ATSR conical scanning design<sup>2</sup> to provide a 1400 km near-nadir view and 750 km inclined view facing backward toward the satellite line of sight. The nominal

---

\*Address all correspondence to: David L. Smith, E-mail: [dave.smith@stfc.ac.uk](mailto:dave.smith@stfc.ac.uk)

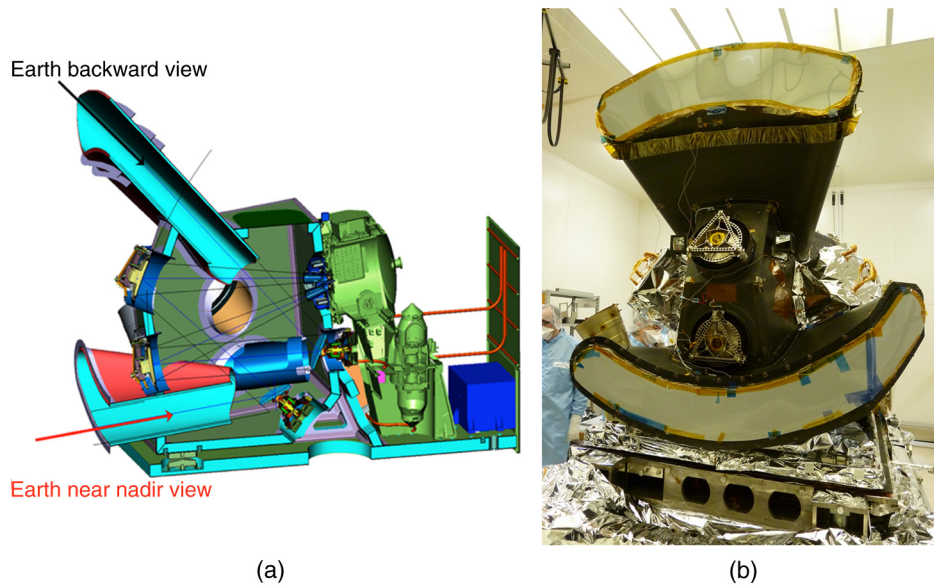


**Fig. 1** (a) SLSTR design concept (b) SLSTR structural thermal model being prepared for testing at RAL.

spectral bands for SLSTR listed in Table 1 are based on those from the ATSR series but include additional short wave infrared (SWIR) bands (S4, S6) for improved daytime cloud detection and thermal channels with dynamic range up to 500 K for fire detection (S7F, S8F). A more detailed description of SLSTR and its expected performance is described in Refs. 3–5.

There are some notable design differences between advanced along track scanning radiometer (ATSR) and SLSTR that affect the calibration of the instrument. First, SLSTR has two telescope/scanners compared to one for ATSR. Although the optical design and coatings for each telescope are identical, they must be calibrated independently to account for the different optical performances and thermal background. Second, unlike ATSR, which had only one detector element per channel aligned behind a common field stop that defined the instantaneous field of view (IFOV), SLSTR has 2, 4, or 8 detector pixels per channel depending on the wavelength and spatial resolution of the channel (see Table 1) that are optically aligned with respect to channel S3. This

**Table 1** Sea and land surface temperature radiometer (SLSTR) spectral bands.

| Band number | Central wavelength ( $\mu\text{m}$ ) | Bandwidth ( $\mu\text{m}$ ) | Spatial resolution at nadir (km) | Function                    | Detector pixels per channel |
|-------------|--------------------------------------|-----------------------------|----------------------------------|-----------------------------|-----------------------------|
| S1          | 0.555                                | 0.020                       | 0.5                              | Chlorophyll                 | 4                           |
| S2          | 0.659                                | 0.020                       | 0.5                              | Vegetation index            | 4                           |
| S3          | 0.870                                | 0.020                       | 0.5                              | Vegetation index            | 4                           |
| S4          | 1.375                                | 0.015                       | 0.5                              | Thin cirrus cloud detection | 8                           |
| S5          | 1.610                                | 0.060                       | 0.5                              | Clouds, fire                | 8                           |
| S6          | 2.225                                | 0.050                       | 0.5                              | Clouds, fire                | 8                           |
| S7          | 3.700                                | 0.380                       | 1.0                              | Night-time SST, fire        | 2                           |
| S8          | 10.850                               | 0.900                       | 1.0                              | SST/LST                     | 2                           |
| S9          | 12.000                               | 1.000                       | 1.0                              | SST/LST                     | 2                           |
| S7F         | 3.700                                | 0.380                       | 1.0                              | Fire                        | 2                           |
| S8F         | 12.000                               | 0.900                       | 1.0                              | Fire                        | 2                           |

does not affect the overall calibration strategy since the calibration sources are common to all detectors, but that coefficients need to be provided for each pixel and viewed separately.

The purpose of this paper is to present the overall calibration strategy for the SLSTR instrument covering the calibration model and initial uncertainty estimates, on-board calibration systems, preflight calibrations, and the characterization testing moving toward the postlaunch monitoring needed to maintain the calibration. At the time of writing it was not possible to provide test results in this paper since the prelaunch tests had not been performed. Results from the prelaunch calibration will be presented in future publications.

## 2 Sea and Land Surface Temperature Radiometer Calibration Approach

The basic principle of radiometric calibration is to equate the output signals, DN, from the sensor to the Earth scene radiance,  $L_{\text{scene}}$ . The quality of the radiometric calibration is determined by the uncertainty in the measured scene radiance,  $u(L)$ . The signal measured by each channel is converted to a voltage and then digitized at 14 bit (in the range 0–16383) such that

$$\text{DN}_{\text{scene}} = F_{\text{ADC}} \{ V [ A\Omega (\tau_{\text{opt}} L_{\text{scene}} + (1 - \tau_{\text{opt}}) L_{\text{inst}}) ] + V_{\text{off}} \}, \quad (1)$$

where  $F_{\text{ADC}}$  = conversion factor for ADC,  $\tau_{\text{opt}}$  = transmission/reflectance of optics,  $A\Omega$  = throughput of optical chain, and  $V$  = voltage output as a function of photons at the detector, this will be a function of detector + amplification and could be nonlinear with photon flux. The response will also be sensitive to instrument polarization.

$L_{\text{inst}}$  = radiance signal emitted from the instrument. For solar reflectance channels, this should be zero

$$V_{\text{off}} = \text{offset voltage.}$$

This reduces to

$$\text{DN}_{\text{scene}} = g(L_{\text{scene}}) + \text{DN}_{\text{offset}}, \quad (2)$$

We invert this to get the scene radiance as a function of DN such that

$$L_{\text{scene}} = g^{-1}(\text{DN}_{\text{scene}} - \text{DN}_{\text{offset}}). \quad (3)$$

SLSTR uses a two-point calibration scheme with sources of known radiance  $L_1$  and  $L_2$  producing average signals  $\langle \text{DN}_1 \rangle$  and  $\langle \text{DN}_2 \rangle$ , so assuming the response is linear with radiance (or at least adjusted for nonlinearity), we obtain

$$L_{\text{scene}} = XL_1 + (1 - X)L_2 + \Delta L_{\text{offset}}, \quad (4)$$

where

$$X = \frac{\text{DN}_{\text{scene}} - \langle \text{DN}_2 \rangle}{\langle \text{DN}_1 \rangle - \langle \text{DN}_2 \rangle}. \quad (5)$$

The term  $\Delta L_{\text{offset}}$  is a residual radiance offset not accounted for by the calibration, due to the stability of the sensor during the calibration period and between calibration observations or unwanted stray light signals. The design of the instrument should ensure that this term is negligible compared to the overall calibration budget.

The combined uncertainty in the radiometric calibration,  $uL$ , can be derived analytically (assuming that the sources of uncertainty are uncorrelated at a first order) using

$$(uL)^2 = \sum_{i=1}^n \left( \frac{\partial L}{\partial a_i} u a_i \right)^2, \quad (6)$$

where for each term  $a_i$ ,  $\partial L / \partial a_i$  the partial derivatives and  $u a_i$  is the uncertainty estimate. The main components of the radiometric calibration budget are given in Table 2.

**Table 2** Principal components of the sea and land surface temperature radiometer (SLSTR) radiometric calibration uncertainty budget.

| Parameter                         | Term                       | Partial derivative   | Characterization   |
|-----------------------------------|----------------------------|--|--|
| Upper calibration source radiance | $uL_1$                     | $\partial L / \partial L_1 = X$  | On-board calibration source calibration and characterization (pre- and postlaunch)                             |
| Lower calibration source radiance | $uL_2$                     | $\frac{\partial L}{\partial L_2} = 1 - X$  |  |
| Digital counts noise              | $uDN$                      | $\frac{\partial L}{\partial DN} = \frac{L_1 - L_2}{(DN_1) - (DN_2)}$             | Signals from onboard calibration sources and prelaunch calibration   |
| Upper calibration source noise    | $u(DN_1)$                  | $\frac{\partial L}{\partial (DN_1)} = X \frac{L_1 - L_2}{(DN_1) - (DN_2)}$       | Signals from onboard calibration sources (negligible since calibration signals are averaged over many samples) |
| Lower calibration source noise    | $u(DN_2)$                  | $\frac{\partial L}{\partial (DN_2)} = (X - 1) \frac{L_1 - L_2}{(DN_1) - (DN_2)}$ |  |
| Nonlinearity                      | $uNL$                      | $\frac{\partial L}{\partial NL} = \frac{L_1 - L_2}{(DN_1) - (DN_2)}$             | Prelaunch calibration  |
| Offset error                      | $\Delta L_{\text{offset}}$ | $\frac{\partial L}{\partial \Delta L_{\text{offset}}} = 1$                       | Analysis and prelaunch calibration   |

Here, the nonlinearity is defined as the relative difference between the actual response and the linear approximation based on calibration at two different signal levels, such that

$$NL = L_{\text{means}} / L_{\text{scene}} - 1, \quad (7)$$

where  $L_{\text{scene}}$  is the scene radiance and  $L_{\text{means}}$  is the measured response. We can invert the calibration equation to derive the nonlinearity as a function of detector voltage, such that

$$NL = DN_{\text{means}} / DN_{\text{scene}} - 1, \quad (8)$$

where  $DN_{\text{scene}}$  is the assumed linear response derived from the calibration signals. Since we employ a two-point calibration scheme for SLSTR, we can assume that the uncertainty due to a nonlinear response tends to zero at the calibration points. In the expected calibration budgets shown in this paper, we have assumed that the nonlinear response has been characterized during the preflight instrument level calibration and what is presented is the residual uncertainty in the measurement. For photoconductive HgCdTe detectors used in the Thermal IR region (TIR), it is known that the detector response “falls off” with increasing photon flux.<sup>6</sup> Essentially, the electron-hole recombination rate increases as the number of carriers (electrons and holes).

**Table 3** Principal components of the uncertainty budget for the blackbody source radiance. Note that the uncertainties for the two calibration sources are treated independently and have to be included in the overall calibration budget in Table 2.

| Parameter  | Term               | Partial derivative   | Characterization   |
|--|--------------------|--|--|
| Emissivity errors  | $u\epsilon$        | $\frac{\partial L}{\partial \epsilon} = L_{\text{bb}} - L_{\text{back}}$   | Prelaunch calibration–BB level and instrument testing          |
| Errors in the background radiance due to blackbody emissivity <1.0 | $uL_{\text{back}}$ | $\frac{\partial L}{\partial T_{\text{back}}} = (1 - \epsilon) \frac{\partial L}{\partial T}  _{T_{\text{back}}}$ |  |
| Blackbody thermometry errors                                       | $uT_{\text{cal}}$  | $\frac{\partial L}{\partial T}  _{T_{\text{bb}}}$  |  |
| Blackbody temperature gradients                                    | $uT_{\text{grad}}$ | $\frac{\partial L}{\partial T}  _{T_{\text{bb}}}$  | Prelaunch calibration and on-orbit measurement of temperatures |
| Blackbody temperature stability                                    | $uT_{\text{stab}}$ | $\frac{\partial L}{\partial T}  _{T_{\text{bb}}}$  | On-orbit measurement of temperatures                           |
| Knowledge of instrument spectral response                          | $u\lambda$         | $\frac{\partial L}{\partial \lambda}  _{T}$  | Prelaunch calibration  |

A nonlinear response may be also due to the design and components used in the detector's amplifier circuit.

This basic approach applies to all spectral channels of SLSTR as described in the following section.

## 2.1 Thermal Infrared

SLSTR employs two cavity BB sources (Fig. 2) whose design is based on the original and now well proven ATSR concept. Each BB consists of a cavity with re-entrant cone geometry, used in conjunction with a high emissivity black coating to provide an emissivity of  $>0.998$ . The cavity is thermally isolated from its support structure to ensure the necessary high thermal uniformity and temperature stability. One BB is heated to  $\sim 300$  K by applying a constant power to a heater coil wrapped around the cavity baffle, while the other "floats" at the opto mechanical enclosure (OME) temperature (nominally  $\sim 250 - 270$  K). Note that the temperatures of the BBs are not actively controlled (i.e., closed loop) to avoid noise from heater switching affecting the calibration. The BBs are positioned ahead of the complete SLSTR optical chain, filling the full optical beam at the intersection of the two scans to ensure that the BBs are viewed for every 0.6 s. The conical scan geometry ensures that the BBs are viewed at the same angle of incidence as the Earth scene, hence, no corrections for view angle are necessary. Also, as with ATSR, because the calibration sources are viewed continuously, no special calibration modes are needed ensuring continuous acquisition of Earth scene data.

The BB radiance, as a function of its temperature, is derived for each spectral band using

$$L_{\lambda, \text{BB}} = \varepsilon_{\lambda} L_{\lambda}(T_{\text{bb}}) + (1 - \varepsilon_{\lambda}) L_{\lambda}(T_{\text{inst}}), \quad (9)$$

where  $L_{\lambda}(T)$  is the in-band radiance integrated over the instrument spectral response function,  $R(\lambda)$ . Hence, the key parameters for this are the cavity emissivity  $\varepsilon(\sum \beta I)_{\lambda} / (\sum \varepsilon_{\lambda} I)$ , cavity temperature  $T_{\text{bb}}$ , the background temperature  $T_{\text{inst}}$ , and the spectral response function.

At IR wavelengths, the spectral radiance  $L(\lambda, T)$  at wavelength  $\lambda$  emitted by a BB at temperature  $T$ , per unit area, per steradian, per unit wavelength is given by the Planck function

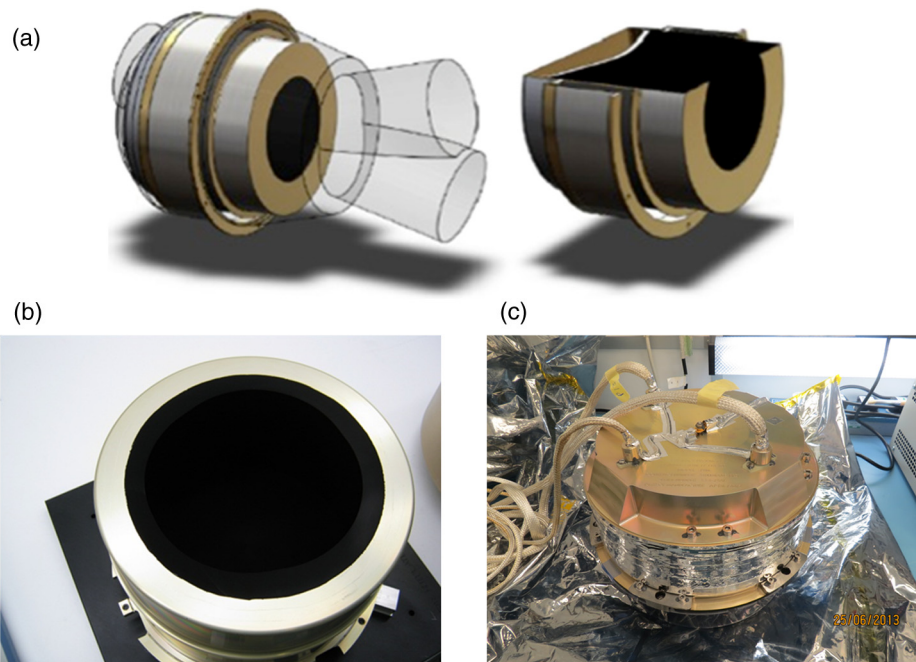


**Fig. 2** (a) Blackbody design for SLSTR, (b) and (c) are the protoflight units, (c) protoflight model blackbody cavity under development (photos courtesy ABSL).

$$L(\lambda, T) = 2 hc^2/\lambda^5 \left( \exp\left(\frac{hc}{\lambda k_b T}\right) - 1 \right), \quad (10)$$

where  $h$  is Planck's constant =  $6.6260755 \times 10^{-34}$  Js,  $c$  is the velocity of light =  $299792458 \text{ ms}^{-1}$ , and  $k_b$  is Boltzmann's constant =  $1.380658 \times 10^{-23} \text{ JK}^{-1}$ .

For an instrument with a spectral response as a function of wavelength,  $R_\lambda(\lambda)$ , the band average radiance is given by

$$L_\lambda(T) = \int R_\lambda(\lambda) L(\lambda, T) d\lambda / \int R_\lambda(\lambda) d\lambda. \quad (11)$$

The black coating is a development of the deep space black that was originally used for the ATSR BBs.<sup>7</sup> Calibration of the cavity emissivity follows the approach used for the ATSR instruments in which witness samples of the black coating were measured at National Institute of Standards and Technology (NIST) and incorporated into a Monte Carlo model to account for the cavity geometry. The model was originally validated for the ATSR BBs by comparing it against a reference BB whose emissivity is higher (i.e.,  $>0.9995$ ).<sup>4</sup> It was found that an accurate measurement of the BB cavity was possible, yet very difficult to achieve in practice. Producing reliable measurements requires a stable and controllable thermal environment and a low-noise radiometer covering the SLSTR IR bandwidths.

The BB temperatures are monitored by five redundant platinum resistance thermometers embedded in the rear part of each BB baseplate, read out by a dedicated BB Electronics Unit (BBEU) comprising a three-wire DC bridge, an amplifier, and analogue to digital converter (ADC) for each sensor. The full chain of thermometers, harnesses, and associated electronics is calibrated with reference to a standard platinum resistance thermometer (PRT) traceable to the international temperature scale of 1990 (ITS-1990).<sup>8</sup> The total uncertainty in the temperature measurement is expected to be  $<20 \text{ mK}$  ( $k = 3$ ) at the beginning of life (BOL).

The background, a reflected component of the BB radiance, is derived from the temperatures of the internal surfaces of the OME that face the aperture of the BB. PRTs mounted on the OME enclosure are read out by a temperature acquisition electronics unit that uses the same readout principle for the BBEU to provide temperature readings to an uncertainty  $<0.2 \text{ K}$  ( $k = 3$ ).

At IR wavelengths, a significant fraction of the measured signal comes from the thermal background of the instrument. Depending on the sensor design, the background signal can be between 10% and 20% of the total signal. Thus, the stability of the thermal background is an integral part of the calibration scheme. To minimize the impact of these variations, the instrument thermal design should ensure that the main optical enclosure is stable around an orbit. Due to satellite design constraints; however, it is not possible to completely eliminate temperature variations; therefore, it is preferable to view the calibration sources as frequently as possible. Hence, we may assume that the uncertainties due to instrument stability,  $\Delta L_{\text{offset}}$ , are negligible compared to the overall calibration budget.

For SLSTR, the spectral responses of all the channels will be measured across the full spectral range to cover any possible out-of-band response, which should be negligible by design. For the purpose of this paper, we assume that the spectral response calibration error is equivalent to a 10 m shift in the peak wavelength. The effect of a spectral response error in the IR channels is indistinguishable to a nonlinear response error (see Fig. 3). As such, the effect of a spectral response error on the radiometric calibration would be accounted for in the characterization of the nonlinearity.

In addition to the instrument's stability, radiometric offsets can be caused by extraneous stray light sources entering the optics. The SLSTR optical design has been optimized to minimize stray light sources from direct solar ingress and other out-of-field sources. A detailed stray light analysis of the instrument has been performed as part of the design process to ensure that the worst case conditions do not affect the overall calibration budget. In the analysis, several causes and sources of stray light are considered including, for example, thermal emission from the Earth view baffles and signals from out-of-field bright sources. For the purposes of this paper, we do not intend to go into a detailed discussion of the analysis of stray light sources, but present a worst case estimate of brightness temperature offset.

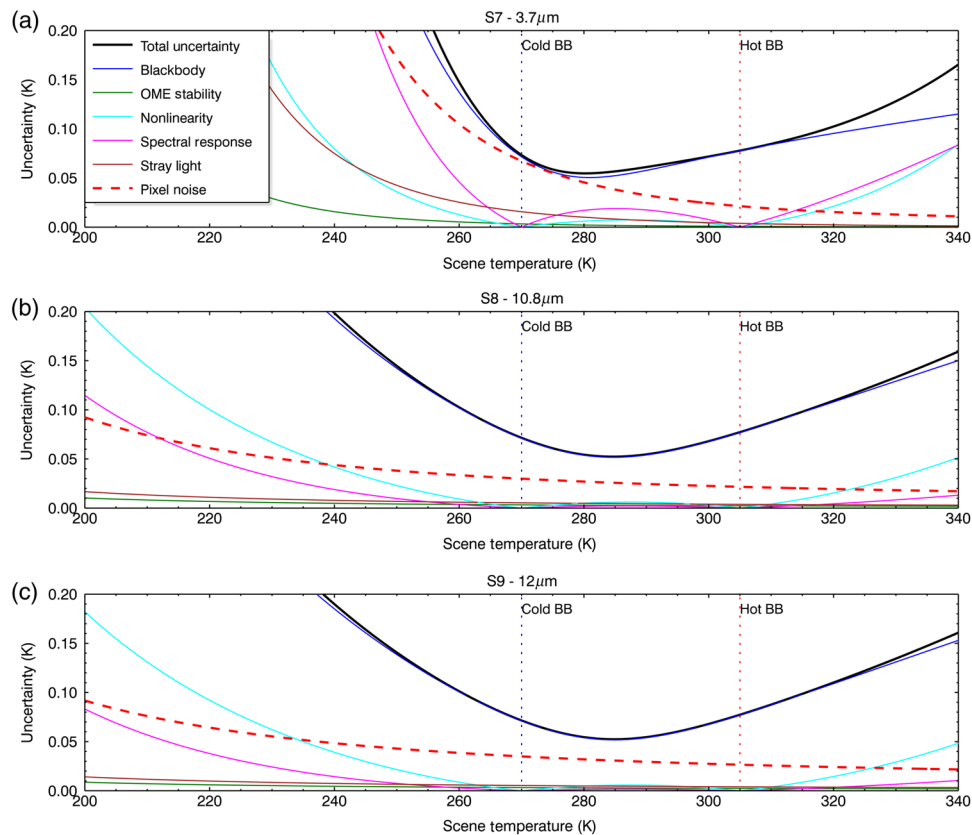


**Fig. 3** Expected beginning of life uncertainty estimates on the SLSTR IR channel radiometric calibration for the  $3.7 \times \mu\text{m}$  (a)  $10.8 \times \mu\text{m}$ , (b) and  $12 \times \mu\text{m}$  (c) channels based on the predicted performance of calibration subsystems. The random pixel noise estimates are based on measurements of the PFM focal plane assembly with EM electronics.<sup>4</sup> Note that the pixel noise is not included in the overall calibration uncertainty since this does not constitute a systematic error. The response nonlinearity is assumed to be 20% but characterized during the preflight calibration to an uncertainty of 1%. The stray light signal shown here represents the worst case situation where the outer edges of the earth view baffles have heated to  $70^\circ\text{C}$  (343 K) as the instrument comes out of eclipse. It is expected that this signal would affect only the edge pixels of the Earth views. In any case, the analysis shows that the stray light signal is small compared to the overall calibration budget .

For the IR channels, the radiometric errors are expressed in terms of an equivalent brightness temperature error, which is derived from the radiance error using Eq. (12)

$$\Delta T = \Delta L \left( \frac{\partial L}{\partial T} \right)_T^{-1}. \quad (12)$$

Combining with the general calibration equation allows us to generate a breakdown of the main sources of uncertainty in the calibration, Fig. 3.

## 2.2 Solar Reflectance Channels

For the visible short wavelength infrared (VIS-SWIR) channels, SLSTR employs a solar diffuser-based visible calibration (VISCAL) system, Fig. 4, following the design approach that was used successfully for ATSR-2 and AATSR.<sup>9</sup> Once per orbit, a white tile diffuser [Zenith®, which is a polytetrafluoroethylene (PTFE)-based material] is illuminated by the sun at normal incidence. The reflected light is directed toward the main instrument telescope by three relay mirrors,  $m_1$ ,  $m_2$ , and  $m_3$ . In the design implemented for SLSTR, the first mirror in the chain after the diffuser,  $m_1$ , is powered slightly to collect light from a smaller area of the

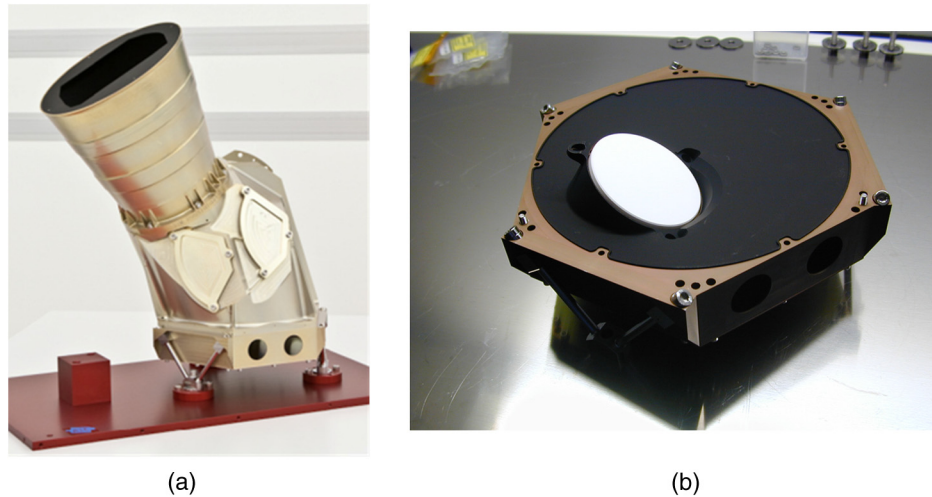


**Fig. 4** (a) SLSTR VISCAL unit (structural thermal model shown) and (b) solar diffuser (photos courtesy TNO).

diffuser. As for the AATSR VISCAL, the relay mirrors are needed to introduce the signal from the diffuser into the main optical chain. A baffle tube is used to restrict stray light from the Earth's atmosphere and the satellite structure. A radiation-hardened glass window (BK7-G18) is mounted at the entrance to the VISCAL to minimize the degradation of the solar diffuser and relay optics by ultraviolet (UV) radiation below 360 nm. The window material was chosen to provide high transmission (>85%) over the SLSTR spectral bands, provide blocking of UV, and be able to withstand degradation due to radiation. Ideally, an on-board monitoring system would be used to monitor the degradation of the VISCAL signals to provide adjustments to the calibration factors. However, the constraints of the instrument accommodation, mass, and power budgets prevented a suitable implementation, such as that implemented for moderate resolution imaging spectroradiometer (MODIS) or visible infrared imaging radiometer suite (VIIRS). Instead, drift monitoring will be performed by means of vicarious calibration monitoring over stable desert and ice targets and by comparison with the ocean and land color imager (OLCI) as implemented for the ATSR instruments.<sup>10</sup>

The dark signal ( $L_2 = 0$ ) is obtained in every scan when viewing the on-board BB sources used for the thermal IR calibration.

As for the IR channels, the conical scanning geometry allows the VISCAL system and BBs to be viewed every scan cycle, so that no special calibration modes for SLSTR are needed, thereby ensuring continuous viewing of the Earth views.

At visible and near-IR wavelengths, the measured top-of-atmosphere (TOA) radiance is given by

$$L_{\text{scene}} = \frac{I_{0,\lambda}}{d^2} R_{\text{scene}}(\theta_0, \theta_v, \varphi_0, \varphi_v) \cos(\theta_0) \text{W cm}^{-2} \text{nm}^{-1}, \quad (13)$$

where  $R_{\text{scene}}$  is the bidirectional reflectance distribution function (BRDF) for the scene, at wavelength  $\lambda$ ,  $I_{0,\lambda}$  is the in-band solar irradiance at 1 AU,  $d^2$  is the Sun–Earth distance correction factor,  $\theta_0$  is the solar zenith angle,  $\theta_v$  is the view zenith angle,  $\varphi_0$  is the solar azimuth angle, and  $\varphi_v$  is the view azimuth angle. The VISCAL system provides a calibration of BRDF  $R_{\text{CAL}}$  that is traceable to a reflectance standard. It is important to note that  $R_{\text{CAL}}$  is not simply the BRDF of the diffuser  $R_D$  but is the product of all the optical components in the optical chain of the VISCAL system and the optical geometry, such that

$$R_{\text{CAL}} = \tau_{\text{UV}} R_D(\theta_0, \theta_v, \varphi_0, \varphi_v) \rho_{m1} \rho_{m2} \rho_{m3} A_{m3} / A_{\text{SLSTR}}, \quad (14)$$

where  $\tau_{\text{UV}}$  is the transmission of the UV window,  $\rho_{m1}$ ,  $\rho_{m2}$ , and  $\rho_{m3}$  are the reflectances of the relay mirrors,  $A_{m3}$  is the aperture area of the relay mirror (the defining aperture of the VISCAL),

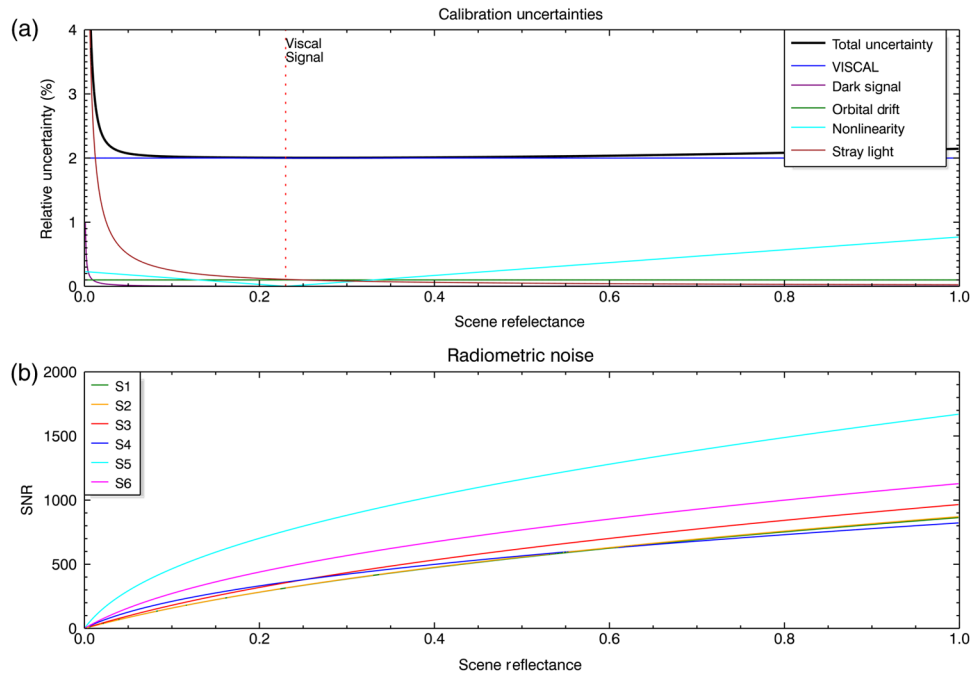


**Fig. 5** Expected beginning of life uncertainty estimates on the SLSTR VIS-SWIR channel radiometric calibration based on predicted performance of calibration subsystems (Channel S1 is shown here). Here, the uncertainty estimates are expressed as a percentage of the measured signal. The random pixel noise estimates expressed as the signal to noise ratio (SNR) are based on measurements of the PFM focal plane assembly with EM electronics.<sup>4</sup> End of life budgets to account for degradations have been considered in the instrument design process, but are not reported here as it is not the purpose of this paper. For the stray light component, the signal has been calculated for a scene with reflectance to  $<0.005$  and assuming an infinite region corresponding to a Lambertian surface with albedo = 1 separated by 1 pixel (i.e., equivalent to a large cloud field adjacent to clear sky over ocean).

and  $A_{\text{SLSTR}}$  is the aperture area of the main SLSTR telescope. Since the diffuser is illuminated at near-nadir incidence, the variation in the BRDF with solar zenith and azimuth angles is small ( $<0.3\%$ ) compared to the overall uncertainty budget of 2%. Nevertheless, the diffuser BRDF was characterized at a component level over the range of view and illumination angles to be used, so that a geometric adjustment can be implemented if needed.

**Table 4** Principle components for the uncertainty budget of the solar channel calibration. Note that this is only part of the overall calibration budget given in Table 2.

| Component                                 | Expression          | Partial derivative   | Characterization   |
|---|---------------------|--|--|
| Reflectance factor for VISCAL             | $uR_{\text{CAL}}$   | $\frac{X}{\cos(\theta_0)}$                                   | Prelaunch calibration–VISCAL and instrument level postlaunch vicarious calibration |
| Degradation of VISCAL reflectance factor  | $uR_{\text{drift}}$ | $\frac{X}{\cos(\theta_0)}$                                   | Postlaunch vicarious calibration   |
| Orbital gain stability                    | $uR_{\text{orbit}}$ | $\frac{X}{\cos(\theta_0)}$                                   | By design and prelaunch testing  |
| Knowledge of instrument spectral response | $uR_{\lambda}$      | $\frac{\partial R_{\text{CAL}}}{\partial \lambda} \approx 0$ | Spectral response (prelaunch)  |
| Solar irradiance error                    | $uI_0$              | 1  | Solspec reference spectrum   |
| Knowledge of instrument spectral response | $uI_{\lambda}$      | $\frac{\partial I_0}{\partial \lambda}$                      | Spectral response (prelaunch)  |

Substituting into the general calibration equation [Eqs. (4) and (13)], we obtain for the Earth scene (assuming  $L_2 = 0$ )

$$R_{\text{scene}} = X \frac{R_{\text{CAL}}}{\cos(\theta_0)}. \quad (15)$$

Conversion to radiance is obtained by multiplying with the in-band solar irradiance that is derived from the reference solar irradiance spectrum of Thuillier et al.<sup>11</sup> taking into account the Sun–Earth distance. The components of the uncertainty budget for the calibration are given in Table 4 and (Fig. 5).

### 2.3 Geometric Calibration

Ortho-geolocation of the SLSTR data requires precise determination of the pixel line-of-sight (LoS) with reference to the satellite reference frame. For SLSTR, the co-registration and alignment stability requirements are particularly demanding to ensure co-registration with the OLCI pixels for the Synergy data products. Unlike OLCI, which has a fixed push-broom geometry, SLSTR has two separate scanners and telescopes that move the detector field of view in a conical scan to achieve the 1400 km swath width. Hence, there is no static LoS for each pixel, but is determined using the geometric calibration model as illustrated in Fig. 6. The instantaneous instrument LoS for each pixel in each view can be determined by a number of rotations and reflections. Each view is a linear transformation and can be represented by a  $3 \times 3$  matrix,  $M$ . Each column of a rotation matrix contains the components of the original basis vectors in the new frame, which are also known as the direction cosines.

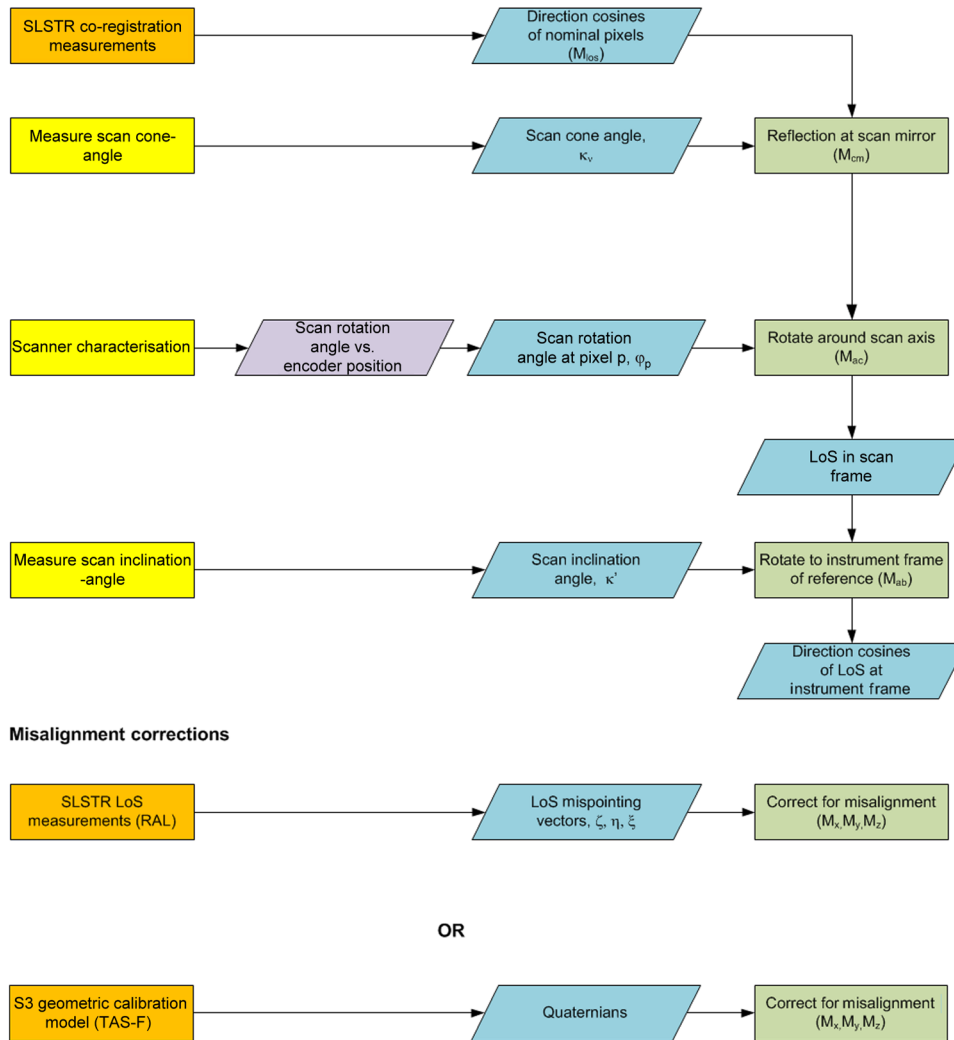
The initial directions of the LoS to the detector elements  $k$  in the respective frames are defined by the direction cosines  $\lambda_k, \mu_k, \nu_k$ . This matrix has three rows and  $k_{\text{max}}$  columns

$$M_{\text{los}} = \begin{pmatrix} \lambda_1 & \lambda_2 & \dots & \lambda_{k_{\text{max}}} \\ \mu_1 & \mu_2 & \dots & \mu_{k_{\text{max}}} \\ \nu_1 & \nu_2 & \dots & \nu_{k_{\text{max}}} \end{pmatrix}. \quad (16)$$

The direction cosines are obtained from the co-registration measurements and represent the pointing offsets between detector LoSs relative to the center of the  $2 \times 1$  km FOV, supposed to be the optical axis of the telescope. For the SLSTR Level-1b products, we only use S3 and S7 and assume that the other channels are co-registered (otherwise the product size becomes very large). The direction cosines are defined as follows:

**Table 5** Breakdown of error sources for LoS model.

| Component                           | Term                           | Characterization           |
|-------------------------------------|--------------------------------|----------------------------|
| Scan cone singles                   | $u\alpha_{\text{cone}}$        | Scanner testing            |
| Scan axes orientation               | $u\alpha_3$                    | Design analysis            |
| Scan rotation angle                 | $u\phi$                        | Encoder readout            |
| Alignment cube orientation          | $u\eta, u\zeta, u\xi$          | Testing at OME level       |
| Interchannel co-registration        | $u\lambda, u\mu, u\nu$         | Instrument level tests     |
| Flip mirror repeatability           | $u\text{LoS}_{\text{flip}}$    | Instrument/subsystem tests |
| Thermo elastic distortion           | $u\text{LoS}_{\text{thermal}}$ | Instrument/OME tests       |
| 0-1g release                        | $u\text{LoS}_{\text{gravity}}$ | By analysis                |
| LoS characterisation                | $u\lambda_i, u\mu_i, u\nu_i$   | Instrument calibration     |
| Alignment with respect to satellite | $u\lambda_S, u\mu_S, u\nu_S$   | Postlaunch calibration     |

**SLSTR LoS model**

**Fig. 6** SLSTR geometric calibration model.

$$\lambda = x/\sqrt{x^2 + y^2 + f^2} \quad \mu = y/\sqrt{x^2 + y^2 + f^2} \quad \nu = f/\sqrt{x^2 + y^2 + f^2}, \quad (17)$$

where  $f$  is the telescope focal length and  $x$  and  $y$  are the centers of the pixels relative to the optical axis at the focal plane of the telescope.

We account for the reflection and rotation at the scan mirror to give the direction cosines relative to each scan axis. The matrix  $M_{cm}$  enables us to take into account the reflection of the scan mirror in the scan reference frame

$$M_{cm}^v = \begin{pmatrix} 1 & 0 & 0 \\ 0 & \cos(\alpha_{cone,v}/2) & -\sin(\alpha_{cone,v}/2) \\ 0 & \sin(\alpha_{cone,v}/2) & \cos(\alpha_{cone,v}/2) \end{pmatrix}, \quad (18)$$

where the cone half angle  $\alpha_{cone}$  is nominally 46.573 deg, and the index  $v$  identifies the view (nadir or oblique). Note that this is independent of the rotation angle of the scan mirror.

The rotation around the scan axis  $\phi$  is obtained by using the matrix  $M_{ac}$ , which represents the scan rotation angle corresponding to each pixel  $p$

$$M_{ac} = \begin{pmatrix} \cos \varphi_p & \sin \varphi_p & 0 \\ -\sin \varphi_p & \cos \varphi_p & 0 \\ 0 & 0 & 1 \end{pmatrix}. \quad (19)$$

Here, the scan rotation angle is obtained from the optical position encoders mounted on the scanner shaft. This represents an advance over ATSR where the scan rotation rate was assumed to be constant with respect to pixel number.

The direction cosines of the LoS relative to the scan axis after reflection at the scan mirror are given by the columns of the matrix

$$M_{los}^s = \begin{pmatrix} \lambda_1^s & \lambda_2^s & \dots & \lambda_{k \max}^s \\ \mu_1^s & \mu_2^s & \dots & \mu_{k \max}^s \\ \nu_1^s & \nu_2^s & \dots & \nu_{k \max}^s \end{pmatrix} = M_{ac}^{-1} M_{cm}^{-1} \begin{pmatrix} -1 & 0 & 0 \\ 0 & -1 & 0 \\ 0 & 0 & 1 \end{pmatrix} M_{cm} M_{ac} M_{los}. \quad (20)$$

Then, the orientation of the scan axis relative to the instrument frame is taken into account. For the oblique view, the scan rotation axis is nominally parallel to the  $-z$  axis of the instrument (toward the subsatellite point), hence, no rotation is needed. For the nadir view, the scan axis is tilted by  $\alpha_3 = 41.097$  deg relative to the instrument frame; therefore, we perform a further rotation to obtain the direction cosines for each pixel in the instrument reference frame

$$M_{ab}(-\alpha_3) = \begin{pmatrix} \cos \alpha_3 & 0 & \sin \alpha_3 \\ 0 & 1 & 0 \\ -\sin \alpha_3 & 0 & \cos \alpha_3 \end{pmatrix}. \quad (21)$$

The direction cosines for the LoS relative to the instrument frame of reference are

$$M_{los}^i = \begin{pmatrix} \lambda_1^i & \lambda_2^i & \dots & \lambda_{k \max}^i \\ \mu_1^i & \mu_2^i & \dots & \mu_{k \max}^i \\ \nu_1^i & \nu_2^i & \dots & \nu_{k \max}^i \end{pmatrix} = M_{ab} M_{los}^s. \quad (22)$$

Finally, we need to account for the misalignment of the instrument relative to the spacecraft frame of reference. At launch, the misalignments will be based on the fixed offsets obtained from the preflight measurements. In flight, the misalignment of the nominal LoS is replaced by matrices computed from a geometric calibration model where, for each view, there are a number of input quaternion tables, indexed by the date of the year, each being vector of the on-orbit position, satellite position in the Earth reference, and the Sun position in the Earth frame. The quaternions are interpolated and converted to a rotation matrix  $T_{calib}^v(X^v)$  to provide the corrected LoS

$$M_{los}^s = \begin{pmatrix} \lambda_1^s & \lambda_2^s & \dots & \lambda_{k \max}^s \\ \mu_1^s & \mu_2^s & \dots & \mu_{k \max}^s \\ \nu_1^s & \nu_2^s & \dots & \nu_{k \max}^s \end{pmatrix} = T_{calib}^v(X^v) M_{los}^i. \quad (23)$$

Using these direction cosines, time calibrations, and the satellite state vectors, time calibration allows us to compute the intersection of each pixel at the earth's surface to obtain the latitude, longitude, view, and solar geometry.

### 3 Prelaunch Calibration

#### 3.1 Spectral Response

SLSTR is a filter radiometer, hence, in-flight calibration of the instrument spectral response is not feasible, so the calibration will be based on the preflight measurements and estimates of the degradation. The approach to be used for SLSTR is based on that followed for the ATSR instruments, where the spectral responses for all channels were measured at focal-plane array (FPA) level. This method is also appropriate for SLSTR, as the sensor's response is mainly determined by the optical components within the detector assembly (DA). The DA is the mechanical

enclosure that houses the nine SLSTR detectors, which are themselves divided over three optical benches within the assembly. (The uncooled visible channels (S1 to S3) and the cooled SWIR (S4 to S6) and TIR (S7 to S9) bench). Each of the SLSTR detectors is optically co-registered at the common image point for the system, and therefore the light is split using a series of dichroic mirrors and filters to select the waveband of interest. The effect of the foreoptics is to attenuate the throughput and not to modify the spectral response (the OME mirrors are spectrally flat over the SLSTR bands, and their spectral reflectances are well characterized with witness samples).

The SLSTR spectral response measurements will utilize the Science and Technology Facilities Council (STFC) molecular spectroscopy facility based at RAL. The facility is based around a Bruker IFS120HR high-resolution Fourier transform InfraRed spectrometer, with a maximum unapodized spectral resolution of  $0.0015 \text{ cm}^{-1}$ . It has a spectral range of 30,000 to  $40,000 \text{ cm}^{-1}$ , achieved through a combination of sources, beam splitters, and detectors. The spectrometer is evacuated using a turbo molecular pump, which significantly reduces the absorption from water vapor and carbon dioxide within the optic compartments. For the spectral response measurements, the DA will be placed at the exit port of the spectrometer where the SLSTR detectors will observe the modulation pattern (interferogram) as light from an internal source passes through the interferometer. The resultant interference pattern can be processed using a Fourier transform to analyze the spectral components of the measured light. This approach has been employed successfully in 2008 on the AATSR flight spare FPA unit.

To accurately quantify the effect that the instrument has on the spectral shape, a correction must be made of the instrument profile. The spectral profile of the spectrometer itself convolves an instrument function onto the spectral response of the FPA. These variations are primarily caused by the transmissive and reflective properties of the optics within the spectrometer, the spectral emission from the internal light source and the detector used to measure this response. The spectrometer instrument function will be removed by performing a spectral measurement through the same optical path, using a calibrated internal detector.

The DA is placed at the focus of the spectrometer. The beam output from the Bruker spectrometer is designed to overfill the F6.8 beam of the optical input to the DA. This ensures that the beam equally fills all the pixels in each detector channel simultaneously and matches the filter requirements. The spectral calibration of each detector pixel within each channel will be performed with the DA vacuum vessel evacuated to  $<10^{-5}$  and all detectors on. To determine the thermal characteristics of the spectral response of the detectors/filters, the tests will be performed with the cryogenic detectors controlled to (or near to) the nominal flight operational temperature of 86 K (nominal) as well as at 90 and 100 K to provide information to cover possible end-of-life (EOL) conditions.

The spectral calibration sequence will include background measurements with a National Physical Laboratory (NPL) calibrated reference detector before and after each DA calibration. The reference detector measurements are used to correct the spectral response of the spectrometer and any instrument drift.

### 3.2 Infrared Calibration

The TIR radiometric calibration methodology will follow the practices used successfully for the ATSR sensors.<sup>12</sup> Radiometric calibration and instrument performance verification will be performed by measuring the signal channel responses over a range of stable external BB target temperatures from 210 to 320 K. Tests are to be performed under stable thermal balance conditions for the instrument. Ideally, only one of the targets will be varied during a calibration run (mainly nadir), while the other (oblique view target) is maintained at a fixed temperature for reference.

Detailed calibration runs at BOL conditions will be undertaken at the center of nadir and the oblique views, with the target temperature being moved at 5 K intervals from 210 to 315 K. Once the initial capability of the instrument is established, the remaining calibration tests covering a full range of viewed scan swath angles will be performed using a reduced set of target temperatures between 240 and 310 K. The purpose of these tests is to measure any scan-dependent variations; the calibration will be verified at different positions around the scan to cover all nadir and oblique view pixels.

Measurements will also be taken with the external target at approximately the same temperature as each of the on-board BBs to verify calibration at points where no correction for non-linearity is needed. The test will be repeated for different on-board BB heater settings as indicated in the overall test flow.

To ensure that the overall radiometric uncertainty from the sources was below 0.04 K, measurements will be collected only when both target baseplates were drifting at rates below 0.02 K over 5 min, and the temperature gradients across the targets were below 0.02 K.

To verify the stability of the sensor over its lifetime, as well as in normal daily operations, each radiometric test will be performed with SLSTR and the test environment under thermal equilibrium at different thermal conditions; these will include the conditions expected at BOL and EOL, as well as simulated orbital cycles. The orbital simulations will be performed with sources at three fixed temperatures 240, 270, and 310 K for a minimum of two orbits.

In addition, low-radiance measurements will be performed on SLSTR using the nadir view target cooled with liquid nitrogen. When the target temperature reaches  $\sim 90$  K, the LN<sub>2</sub> supply will be disconnected and the BB allowed to warm up slowly; measurements are taken at 1 K intervals throughout the temperature rise. This test is only possible for one view as only one of the external BB sources has an LN<sub>2</sub> loop fitted.

### 3.3 Solar Channel Calibration

The essential objectives of the prelaunch calibration at instrument level are to determine by experimenting the following:

- The VISCAL reflectance factor for each channel  $R_{\text{viscal}}$ . A value for this can be obtained from component measurements (diffuser, mirrors, and geometry) but does not fully account for the coupling to the instrument optical chain.
- A measurement of the end-to-end radiometric response.
- The radiometric noise as a function of scene radiance over the full dynamic range.
- A variation of the radiometric response around nadir and oblique views.
- The polarization sensitivity.

As discussed in Sec. 2.2, the radiometric calibration of the solar channels is traced through the VISCAL system. Hence, the absolute radiometric response of the signal channels is not the primary measurement to be performed on ground but rather the characterization of the VISCAL reflectance factor. This is independent of instrument temperature, since it is primarily a function of the optical properties of the calibration system and not the detector response. Nevertheless, the radiometric response, noise performance, nonlinearity, and polarization sensitivity will be characterized.

For the solar channel calibration, the plan is to perform much of the calibration at instrument level outside the vacuum chamber. Achieving the required radiometric accuracy for the solar channels relies on using light sources that need to be operated in air. Also, the sources will need to be used at different positions around the instrument and used in conjunction with variable apertures. Again the need to reconfigure the source during the testing means that the solar channel calibration is best performed in a clean room.

To allow calibration tests of the VIS-SWIR channels in a dark clean room, the instrument DA is a vacuum vessel to allow the detectors to be cooled to or close to flight representative temperatures. A ZnSe window mounted on the DA allows light to enter the FPA while under vacuum. As with all the calibration measurements, the instrument temperatures along with other key parameters affecting the calibration will be recorded to allow any adjustments for flight conditions if needed.

The primary source to be used for many of the tests of the VIS-SWIR channels is a custom-built 500 mm integrating sphere source with 150 mm exit aperture to cover the full SLSTR optical beam, Fig. 7. The source has six lamps, including one with a variable aperture to provide continuous radiance levels. The source output will be monitored using a combination of stable radiometers and fiber-fed spectrometers, so that the source stability can be accounted for.

In order to support traceability of the integrating sphere radiance measurements to primary standards, RAL has transfer standard absolute radiance source (TSARS) supplied by the UK

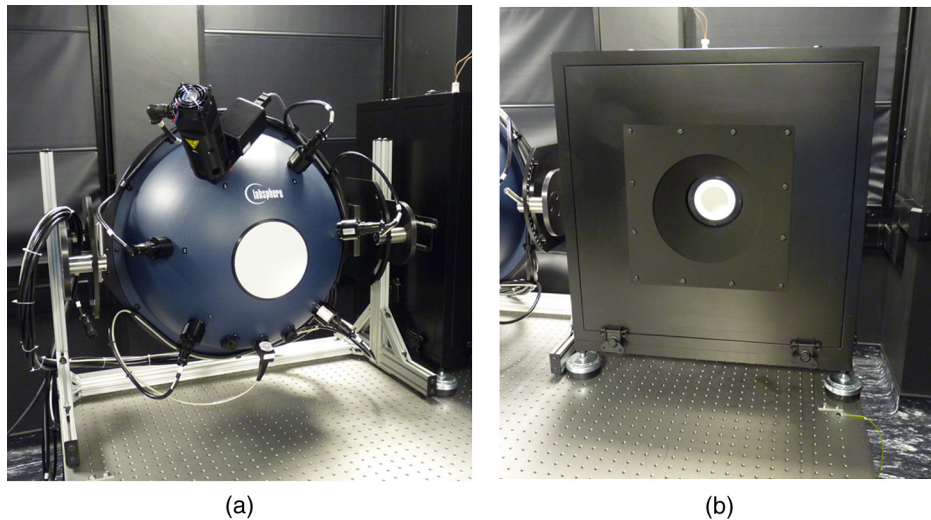


**Fig. 7** (a) 500 mm integrating sphere for SLSTR calibration and (b) transferable standard absolute radiance source (TSARS).

NPL.<sup>13</sup> This type of source was specifically developed by NPL to support the calibration of Earth observation instruments including geostationary earth radiation budget (GERB) and global ozone monitoring experiment 2 (GOME-2). The source consists of an integrating sphere that is illuminated by a number of external lamps. It gives a provision of a high stability reference with which to calibrate the SLSTR solar channels. The TSARS has a uniformity of better than  $\pm 0.4\%$  across the 75 mm diameter exit port.

### 3.4 Geometric Calibration

As outlined in Sec. 2.3, the SLSTR geometric calibration is not based on a single measurement but is dependent on a number of key measurements. The overall SLSTR alignment characterization and verification approach are outlined as follows. The interchannel co-registration and LoS, with respect to the OME-FPA mechanical interface via a gauge, are verified at FPA level.<sup>4</sup> Telescope focal lengths, apertures, scanner cone angles, and alignment to the OME mechanical interface are characterized at the OME level. The scan control law (scanner calibration), including the identification of the encoder positions for the nadir and center of oblique view pixels (in a plane parallel to the XZ plane), scan stability is verified at scan unit level.

A direct LoS measurement is required to verify the pointing vectors of the detectors relative to the instrument reference cube. The angles involved are large (measurement is required at the center and edges of the scan cone and in both nadir and oblique views), hence this is best done using theodolites. However, a theodolite cannot measure the visible detectors directly as they are not reliably visible by eye; therefore, a two-step measurement is made using the FPA shiny diaphragm at the focus of the OME telescopes as a common reference.

In the first stage, theodolites are used to establish the pointing vector of the diaphragm, which can be seen by eye, relative to the instrument reference cubes. In practice, this will be done by measuring the pointing vector with a theodolite at multiple positions along the edges of the diaphragm and at the corners, to allow the center position of the diaphragm to be interpolated. This measurement will be made in each view and at the center and both ends of the scan. It is not possible for a single theodolite to view both the diaphragm and the optical reference cubes, hence two theodolites are used. The technique is illustrated in Fig. 8.

In the second step, the FOV optics (see section below and Fig. 9) will be used to obtain the LoS of the visible detectors relative to the diaphragm. Due to the limited field angle coverage of the FOV optics, this measurement can only be made at the center of the scan cone (with the option to move the scan mirror by  $\pm 1$  km equivalent ground distance) in each view. The pointing vectors in this measurement will be relative ones, which were obtained from angular

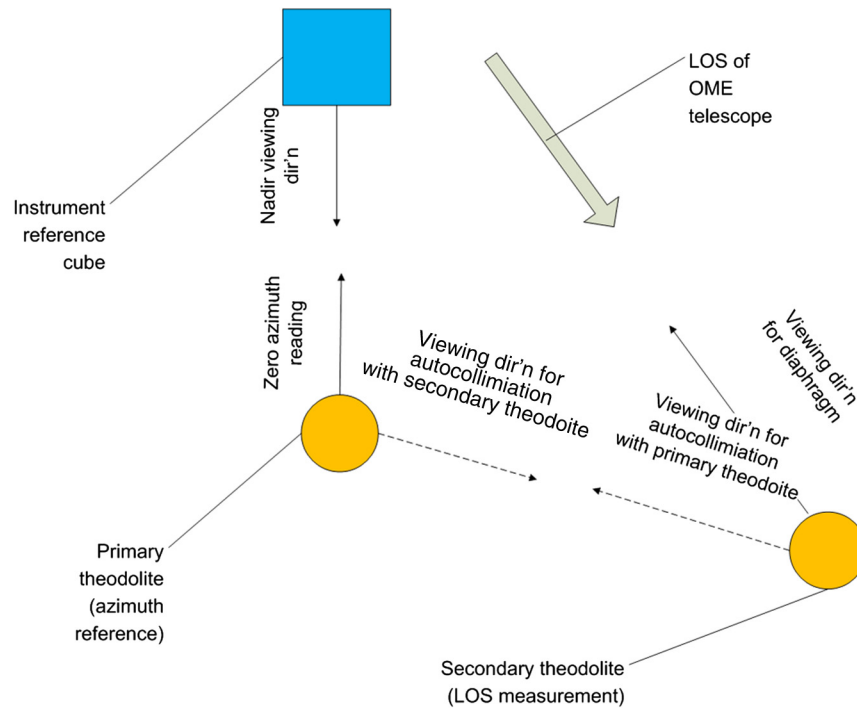


**Fig. 8** Measurement principle of LoS measurement.

displacements of the FOV optics scan mirror. The location of the diaphragm will be measured by viewing the focused spot from the FOV optics in retroreflection along the LoS of the FOV optics, by inserting a pellicle beam splitter and a charged coupled device (CCD) camera at the focus of the off-axis parabola. Because the diaphragm is reflective, it will be possible to view the focused spot from the FOV optics as it is scanned across the edge of the diaphragm onto the detector. Measurements of the scan mirror orientation will be made with the focused spot at multiple positions along the edges of the diaphragm to allow the center of the diaphragm to be found by interpolation. The focused spot will also be scanned across the visible detectors while they are read out and while the scan mirror orientation is recorded. The knowledge of the scan mirror orientations with the focused spot at the diaphragm and at the visible detectors allows the pointing vectors of the visible detectors to be determined relative to the diaphragm.

Combining the two measurements allows the LoS of the visible detectors to be calculated for all of the scan angles and views addressed by the theodolite measurement in the first step, using the diaphragm pointing vector as a common reference to link the two measurements.

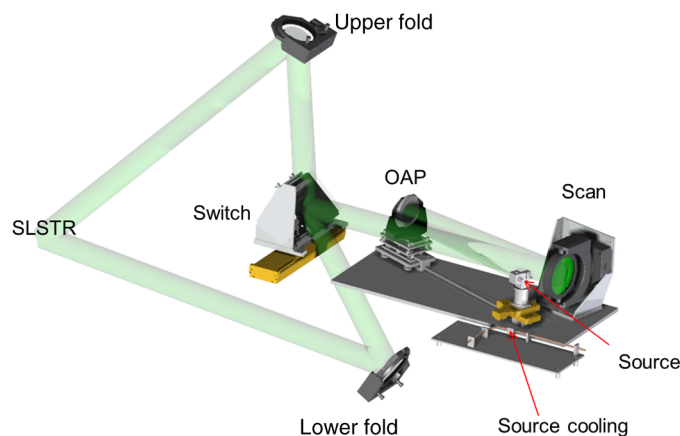


**Fig. 9** Optical layout of test equipment to be used for the SLSTR FOV tests.

In the third step, the scan across the visible detectors is repeated with the instrument in vacuum at ambient temperature. The previous measurement is made with the instrument and FOV optics in the vacuum chamber in air, so that there is no mechanical disturbance between the two measurements. This step enables the air-to-vacuum changes in LoS to be assessed.

The IFOV of each channel will be mapped out by scanning the image of a point source across the focal plane at the shiny diaphragm and by recording the detector's response as a function of position. While the instrument's scan mirror is kept stationary, the image of the point source is steered across the field in both azimuth and elevation by a gimbal-mounted optical flat (Fig. 9). This method proved to be the most reliable way of mapping the IFOV for all ATSR co-registrations, IFOVs, subsampling angles and MTFs are obtained from the scan data. These tests will be performed after thermal vacuum cycling at BOL and EOL steady-state conditions.

### 3.5 Calibration Rig

A purpose-built calibration rig has been designed, built, and verified to test and calibrate the Sentinel-3 SLSTR instruments, Fig. 10. The design is based on the principle of two trolleys: one to accommodate the instrument under test and the other for the calibration equipment.

The instrument trolley is used to support the instrument inside the space test chamber (STC) for IR radiometric calibration and FOV testing, and outside STC, during visible and SWIR testing. The instrument trolley and calibration trolley locate with each other within STC to give repeatable alignment of the instrument to the calibration equipment during the tests held within the chamber. The instrument trolley structure consists of a welded aluminum alloy framework, made from open section members for ease of initial cleaning, and thereafter maintaining the high cleanliness levels required. The instrument is mounted on an invar plate representing the mechanical and thermal interfaces of the spacecraft.

The calibration trolley supports the BBs as well as their related mechanisms, the FOV calibration optics, and thermal hardware. The framework is mounted on flanged wheels to allow the complete assembly to be wheeled into the STC. This simplifies the integration process and ease of access to the test equipment.

The BBs to be used for SLSTR are those originally designed and built for ATSR-1. They are approximately 350 mm high and 250 mm in diameter and weigh 20 kg each. Some refurbishment of the BBs has been performed to adapt to the SLSTR rig, including replacing multilayer insulation, and modifying the mounting features so that they can be attached at the front rather than the rear. No modifications have been made that affect the radiometric performance thereby ensuring continuity with the ATSR series.

Each BB is required to move in an arc to match the scanning angles of the instrument. These motions are provided by commercial curved rail systems and are made from stainless steel or

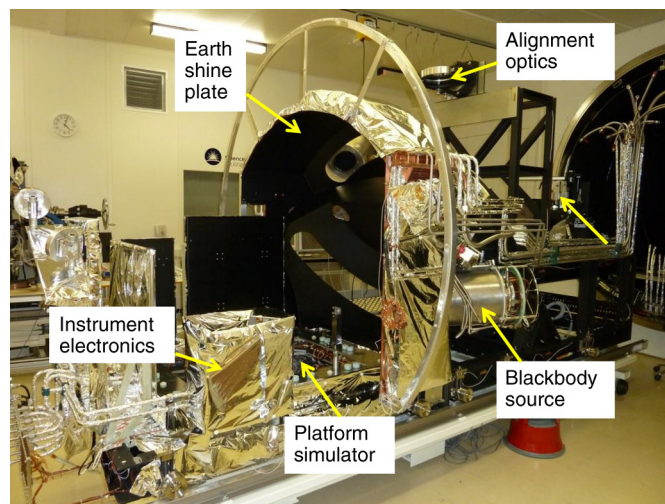


Fig. 10 SLSTR calibration rig under preparation for thermal testing.

coated carbon steel. The mounting holes in the rails allow sufficient adjustment and co-alignment of the BBs. Each BB is attached, via a thermally isolating support, to a carrier fitted with wheels that engage with the “V” profile of the curved rail. The carrier also houses a stepper motor, gearbox, and drive pinion that meshes with teeth incorporated into the rail. The position of the BB along its track is controlled by counting the steps of the motor.

Earth thermal radiation is simulated by an Earthshine plate designed to operate between 60°C and +50°C that comprises rolled copper plates with copper pipes brazed to the back. The assembly is mounted on thermally isolating stand-offs attached to the calibration trolley, with additional electrical grounding wires. The pipework is arranged to provide even cooling when the cooling fluid is circulated. The liquid is fed in at the lowest point and drawn off at the highest points, allowing air to be vented from the system. During commissioning tests with the structural thermal model (STM), the earth shine simulator (ESS) remained stable to  $\pm 0.5^\circ\text{C}/\text{hr}$  with temperature gradients of  $<0.5^\circ\text{C}$  across the full area. For the orbital simulation tests, the required rate of  $1.1^\circ\text{C}/\text{minute}$  for cooling and warm-up was successfully achieved.

Thermal radiator targets mounted on the instrument structure are used to simulate the view to space. These are cooled by LN<sub>2</sub> with heaters to provide fine control of the temperatures. The tests with the STM demonstrated that the facility was able to provide the correct interface temperatures needed to maintain the instrument at flight operating temperatures needed for calibration.

The calibration sources, translation stage motors, and filter mechanisms will be controlled via a test facility control system (TFCS). The TFCS will be based on the system currently used for the SLSTR prelaunch calibration facility that controls and monitors the calibration sources, optics, mechanisms, and thermal hardware. The system allows commands to be received from the instrument electrical ground support equipment (EGSE) via an ftp router. Data from the equipment are logged internally by the test facility control system (TFCS) but are also transmitted into the instrument EGSE in Consultative Committee for Space Data Systems (CCSDS) packet format.

For each test, the equipment will be driven from a test script that defines the source configuration, monitoring conditions, and the measurement steps, for example, mirror movement and filter position. These are essentially configured spreadsheets that are unique for each test.

## 4 Postlaunch Activities

The calibration of SLSTR will be maintained on-orbit through sustained activities as for the Envisat missions.

For the solar reflectance channels, methods developed for the AATSR mission will be employed to monitor the degradation of the VISCAL system and to verify the calibration against reference sensors.<sup>9</sup> Of particular interest, the use of bright desert and ice targets is to perform intercomparisons. Here, cloud free-top of atmosphere (TOA) reflectances are extracted from the L1b products and compared with those of other sensors, taking into account the view/solar geometry, spectral differences, and atmospheric conditions.

The Committee for Earth Observing Systems Infrared Visible Optical Subgroup (CEOS-IVOS) instigated a working group to assess how vicarious calibration approaches performed by different institutes compared when using a common reference dataset.<sup>14</sup> In this study, three sites were selected, the Libya-4, Niger-2, and Dome-C sites for which a time series of cloud-screened TOA reflectance for the sites were generated. The sensors under study were AATSR, MERIS, MODIS-Aqua, POLDER-3, and VEGETATION-2 covering the years 2006 to 2009. Each institute independently applied their respective methods to the reference dataset to produce comparisons of TOA reflectance. The results were able to demonstrate that the uncertainties in the comparisons of the order  $\sim 1\%$  were achievable, particularly for sensors with similar spectral bands and view geometry.

For the thermal IR channels, the calibration traceability is via the on-board BBs as described in Sec. 2.1. Direct verification of the Level-1 calibration to the uncertainties required ( $<0.1\text{ K}$ ) is not feasible at these wavelengths. Nevertheless, comparisons between individual SLSTR instruments and with other satellite instruments (e.g., AVHRR, IASI, and VIIRS) will be performed to

validate the IR radiometric calibrations of individual instruments and to ensure the consistency and continuity of the climate temperature dataset. In flight, calibration of the fire channels will be performed using Sun-glint scenes using an algorithm originally derived to calibrate the ATSR-1/2 1.6  $\mu\text{m}$  channel from the 3.7  $\mu\text{m}$  channel.<sup>15</sup>

For an intercomparison in radiance to be meaningful, the observations from different instruments must be closely matched in position, time, viewing geometry, and spectral response. When all four conditions are met, simple comparisons can be made (e.g., between the ATSR-series instruments). Where there are significant differences, these must be corrected with suitable atmospheric and surface models, which may require additional information about the local state.

Intercomparisons are particularly important during overlap periods, when succeeding instruments take over primary responsibility for observations, but can also be undertaken throughout the instrument lifetime wherever suitable matched data are available. When instrument ground tracks are not identical, this may only occur with any frequency at high latitudes and where ascending and descending orbit segments cross.

Surface *in-situ* measurements provide a further source of validation information. They are, however, separated from the instrument by the atmospheric path and must be treated as inputs to atmospheric and, if required, surface models to reproduce the TOA radiances observed by the satellite. For Level 1 intercomparisons, observations must be closely matched in position, time, and, if relevant, spectral response. More commonly, *in situ* observations are intercompared with Level 2 products. For SLSTR as with AATSR, a key method will be to use ship-borne radiometers, such as SISTeR.<sup>16</sup>

## 5 Conclusions

In this paper, we have presented an overview of the calibration of the SLSTR instruments. Many of the features of the calibration concepts and planning are based on the many years' experience from the ATSR program to ensure continuity of the data quality. At the time of writing, the calibration campaign of the first flight instrument is expected to be performed in late 2014. This will be a three-month campaign involving 24-h working to ensure that the instrument has been fully characterized prior to launch. The results of the measurements will form the basis of the instrument characterization database that will be utilized by ground processing. Sustained on-orbit activities will ensure that the calibration is maintained throughout the lifetime of the mission.

## Acknowledgments

The authors would like to thank the team at RAL Space who are responsible for the many aspects of the design, analysis, and commissioning tests for the calibration facility. The SLSTR calibration activities are funded through the ESA Sentinel-3 mission project.

## References

1. C. Donlon, "The global monitoring for environment, and security (GMES) Sentinel 3 mission," *Remote Sens. Environ.* **120**, 37–57 (2012).
2. T. Edwards et al., "Description of ATSR the along track scanning radiometer: measurement of sea-surface temperature from ERS-1," *JBIS-J. Brit. Interpla.* **43**, 160–180 (1990).
3. B. Coppo et al., "SLSTR: a high accuracy dual scan temperature radiometer for sea and land surface monitoring from space," *J. Mod. Opt.* **57**(18), 1815–1830 (2010).
4. P. Coppo et al., "The sea and land surface temperature radiometer (SLSTR) detection assembly design and performance," *Proc. SPIE.* **8889**, 888914 (2013).
5. G. J. Hawkins et al., "Cooled infrared filters and dichroics for the sea and land surface temperature radiometer (SLSTR)," *Appl. Opt.* **52**(10), 2125–2135 (2013).
6. E. Theocharous, J. Ishii, and N. P. Fox, "Absolute linearity measurements on HgCdTe detectors in the infrared region," *Appl. Opt.* **43** 4182–4188 (2004).
7. I. M. Mason et al., "Blackbody calibration sources of high-accuracy for spaceborne infrared instrument: the along-track scanning radiometer," *Appl. Opt.* **35**, 629–639 (1996).

8. H. Preston-Thomas,, “The international temperature scale of 1990 (ITS-90),” *Metrologia* **27**, 3–10 (1990).
9. D. L. Smith, P. D. Read, and C. T. Mutlow, “The calibration of the visible/near infra-red channels of the along-track scanning radiometer-2 (ATSR-2) in sensors, systems and next-generation satellites,” *Proc. SPIE*. **3221**, 53–62 (1997).
10. D. L. Smith and C. V. Cox, “(A)ATSR solar channel on-orbit radiometric calibration,” *IEEE Trans. Geosci. Remote Sens.* **51**(3), 1370–1382 (2013).
11. G. Thuillier et al., “The solar spectral irradiance from 200 to 2400nm as measured by the SOLSPEC spectrometer during the Atlas and Eureka missions,” *Sol. Phys.* **214**(1), 1–22 (2003).
12. D. L. Smith et al., “ATSR infrared radiometric calibration and in-orbit performance,” *Remote Sens. Environ.* **116**, 4–16 (2012).
13. E. R. Woolliams et al., “Improved transfer standard sources for calibration of field spectrometers used for Earth observation applications,” *Proc. SPIE* **4881**, 386–394 (2002).
14. M. Bouvet et al., “Intercomparison of vicarious calibration methodologies and radiometric comparison methodologies over pseudo-invariant calibration sites,” Report to the CEOS/IVOS working group (2012), <http://calvalportal.ceos.org/ceos-wgcv/ivos/wg4/final-report>
15. A. M. Zavody et al., “A novel method for calibrating the ATSR-2 1.6-um channel using simultaneous measurements made in the 3.7-um channel in sun glint,” *J. Atmos. Ocean. Techn.* **15**, 1243–1252 (1998)<http://journals.ametsoc.org/doi/abs/10.1175/1520-0426%281998%29015%3C1243%3AANMFCT%3E2.0.CO%3B2>
16. T. J. Nightingale, “The SISTeR validation radiometer,” [http://www.atsr.rl.ac.uk/validation/sister/sis\\_inst/index.shtml](http://www.atsr.rl.ac.uk/validation/sister/sis_inst/index.shtml).

**David Smith** obtained a BSc degree and then a PhD in physics at Royal Holloway College, University of London. In 1991 he moved to Oxford University, where he worked as calibration scientist for the Along-Track Scanning Radiometer-2. Since 1994, he has worked at the RAL working on the pre- and postlaunch calibration of satellite instruments, including ATSR-2, AATSR and lately SLSTR. He is an active participant in the CEOS IVOS working group.

Biographies of the other authors are not available.